Accepted Manuscript

Tm^{3+} doped barium molybdate: A potential long-lasting blue phosphor

Ana Paula de Azevedo Marques, Roseli Künzel, Nancy K. Umisedo, Renato Mazin Latini, Elizabeth Mateus Yoshimura, Emico Okuno

PII: S0925-8388(17)33661-7

DOI: 10.1016/j.jallcom.2017.10.225

Reference: JALCOM 43622

To appear in: *Journal of Alloys and Compounds*

Received Date: 4 August 2017

Revised Date: 23 October 2017

Accepted Date: 24 October 2017

Please cite this article as: A.P.d.A. Marques, R. Künzel, N.K. Umisedo, R.M. Latini, E.M. Yoshimura, E. Okuno, Tm^{3+} doped barium molybdate: A potential long-lasting blue phosphor, *Journal of Alloys and Compounds* (2017), doi: 10.1016/j.jallcom.2017.10.225.

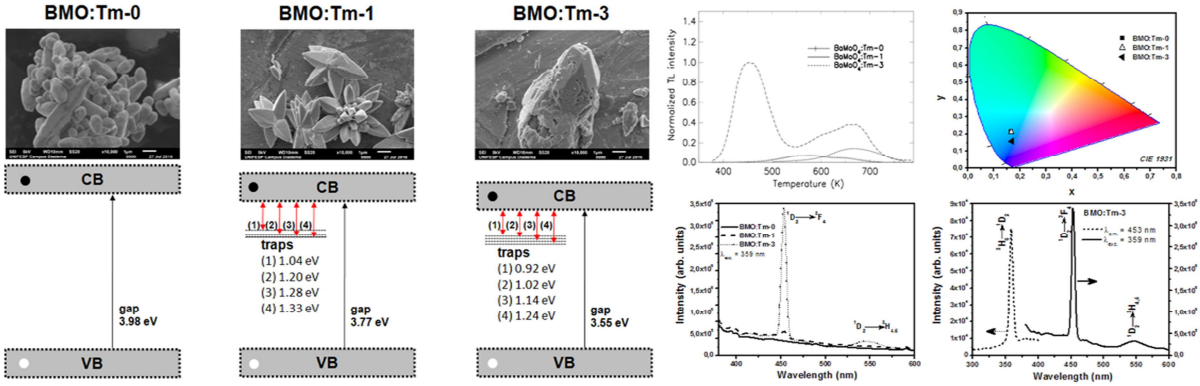

Tm^{3+} doped barium molybdate: A potential long-lasting blue phosphor

Ana Paula de Azevedo Marques[a], Roseli Künzel[b], Nancy K. Umisedo[c], Renato Mazin Latini[a], Elizabeth Mateus Yoshimura[c], Emico Okuno[c]

[a] *Universidade Federal de São Paulo - UNIFESP, Departamento de Química, R. São Nicolau, 210 - Centro, Diadema - SP, CEP 09913-030 Brazil*
[b] *Universidade Federal de São Paulo - UNIFESP, Departamento de Física, R. São Nicolau, 210 - Centro, Diadema - SP, CEP 09913-030 Brazil*
[c] *Universidade de São Paulo, Instituto de Física, Cidade Universitária, CEP 05508-900, São Paulo, SP, Brazil*

Abstract

Molybdates have applications in various fields such as phosphors, optical fibers, scintillators, magnets, sensors and catalysts. Thulium ion is an excellent blue activator and plays an important role in the design of persistent luminescent materials. This paper reports the investigation of the structural and luminescent properties of Barium Thulium Molybdate $(Ba_{1-x}Tm_x)MoO_4$ microcrystals (with x = 0, 0.01 or 0.03). The scheelite-type crystalline structure was identified from XRD and Raman studies. Under ultraviolet (359 nm) excitation, photoluminescence (PL) spectra present the characteristic emission bands at 453 nm and 545 nm which are due to the $^1D_2 \rightarrow {}^3F_4$ and $^1D_2 \rightarrow {}^3H_{4,5}$ transitions, respectively, from Tm^{3+} ions. Thermoluminescence (TL) measurements were performed with powdered samples previously irradiated with beta radiation. The depth of traps, associated with trap levels located inside the band-gap, was determined from TL data using different methods of glow curve analysis. The kinetic parameters, determined from thermoluminescent glow curves, provide evidence about a possible persistent luminescence emission from the $(Ba_{0.97}Tm_{0.03})MoO_4$ sample. This is a potential blue-light or ultraviolet long-lasting phosphor, with a trapping level lifetime, at room-temperature (300 K), of about 6 days.

Keywords: Ceramics, Luminescence, Microwave, Rare Earth Alloys and

1. Introduction

Barium Molybdates ($BaMoO_4$) have attracted increasingly attention as a host material for designing novel optical devices due to their thermal and chemical stabilities as well as their efficient energy transfer from the tetragonal molybdate group (MoO_4^{-2}) to dopant ions [1, 2, 3]. Molybdates have a scheelite-type crystalline structure and allow doping with trivalent rare-earth ions, which result in excellent luminescent properties, enabling the light emission of a variety of colors [2, 3, 4, 5, 6]. Among rare earth ions, Tm^{3+} is employed by researchers in the design of blue emitting phosphors [2, 7, 8, 9, 10], white light emitting diodes [11, 12, 13] as well as field-emission display (FED) devices[14]. Tm^{3+} ions also play an important role on the design of persistent luminescent materials. The use of Tm^{3+} as a co-doping ion in $Ca_2Si_5N_8$:Eu^{2+} and $Ba_2MgSi_2O_7$:Eu^{2+} phosphors showed an enhancement of the persistent luminescence emission, increasing both the intensity and duration of light emission [15, 16]. Cho (2016) investigated the light emission from a $BaMoO_4$:Tm^{3+} phosphor, which occurs in the blue spectral range with a tetragonal crystal structure[2]. However, to our present knowledge, the influence of Tm^{3+} doping concentration on the $BaMoO_4$:Tm^{3+} emission and the investigation about the luminescent behavior, regarding the determination of traps parameters, have not yet been reported.

The optical properties of luminescent materials are influenced by defects or impurity sites called traps located inside the band-gap [17, 18]. These defects can be caused by chemical reactions during the fabrication process, alio-valent co-doping of the material, unidentified lattice defects and distortions or defects generated by radiation exposure [19, 20, 21, 22, 23].The exposure of the phosphor to ultraviolet or ionizing radiation generates electron-hole pairs which can get trapped in these states located inside the band gap of the material, remaining in these traps until they acquire sufficient energy from an external heat or

light source to escape [17, 23, 24]. The required energy for releasing these electrons, the trap depth, provides information about some luminescence features [25, 26, 27]. For materials with very shallow traps the observed afterglow is short, whereas, for those which present deep traps, no charge carriers can escape at room temperature [25, 27]. The light emission resulting from gradual release of the charge carriers from these trapping centers is called persistent luminescence[15, 28, 29]. Persistent luminescent materials present traps with depth values ranging around 0.58 to 1.13 eV, associated with a physically appropriated frequency factor value, resulting in light emission in the ultraviolet, visible or infrared spectral ranges lasting from minutes to days after ceasing the excitation [27, 30, 31, 32].

In this work, we present surface and luminescent investigations of Thulium-Doped Barium Molybdate $(Ba_{1-x}Tm_x)MoO_4$ microcrystals (with $x = 0$, 0.01 or 0.03), synthesized by a coprecipitation method and grown in a microwave-assisted hydrothermal (MAH) system. Microstructural characterization has been performed using XRD, Raman and SEM techniques. Photoluminescence and Thermoluminescence measurements have been carried out in order to get information about the luminescence behavior and trap kinetics in these compounds.

2. Materials and Methods

2.1. Materials

All chemical reagents were analytical grade and were used without further treatments: molybdenum trioxide (MoO_3) (Alfa Aesar, 99.95%), barium acetate ($Ba(CH_3CO_2)_2$) (Alfa Aesar, 99%), thulium (III) oxide (Tm_2O_3) (Aldrich, USA, 99.9%) and polyethylene glycol ($HOCH_2CH_2OH$) (Mw. 200) (PEG 200) (Sigma-Aldrich, 99.9%).

2.2. Synthesis of Barium molybdate $BaMoO_4$:Tm^{3+})

$BaMoO_4$:Tm^{3+} (with 0, 1 and 3 mol% Tm^{3+}, in relation to barium ions) were synthesized using the microwave-assisted hydrothermal (MAH) method.

For this synthesis, molybdenum trioxide (5x10^{-3} mol) was dissolved in 50 mL of distilled water with vigorous stirring. The pH of the solution was adjusted to 12 by adding KOH. ($Ba(CH_3CO_2)_2$) (5x10^{-3} mol) and thulium nitrate were added under constant stirring. Thulium nitrate reagent was produced previously by adding nitric acid to thulium oxide (III) at 70 ^{o}C. Then, 1.5 mL of a capping reagent, PEG 200, was added. The systems were hydrothermally treated using the MAH method. Reaction systems were transferred into a sealed teflon autoclave and placed in an adapted domestic microwave (2.45 GHz, maximum power of 800 W), heat treated at 100 ^{o}C for 16 min with a heating rate fixed at 100 ^{o}C/min. The pressure in the sealed autoclave was stabilized at around 2.0 atm. The autoclave was cooled to room temperature naturally, and the resulting white precipitate was collected, washed with water and ethanol and dried at 60 ^{o}C. Hereafter, the $(Ba_{1-x}Tm_x)MoO_4$ (x = 0; 0.01 or 0.03) samples will be referred to as BMO:Tm-0 (x=0), BMO:Tm-1 (x=0.01) and BMO:Tm-3 (x=0.03).

2.3. Characterization of $BaMoO_4$ samples

The samples were characterized by XRD using a Rigaku-DMax/2500PC (Japan) with $Cu - K_\alpha$ radiation (λ = 1.5406 Å) in the 2θ range from 5° to 75° with a 0.02^o/min increment. Lattice parameters and unit cell sample volumes were calculated using the least-square refinement REDE93 program. The average crystallite diameter (D_{crys}) of the materials after hydrothermic treatment was determined by XRD results with the (112) diffraction peak of the $BaMoO_4$ phase located around 26.6^o according to the procedure described elsewhere [4]. Raman spectra were recorded using a Raman Renishaw microscope, inVia model, with multichannel CCD detector and He-Ne laser (632.8 nm), set to 0.17 mW at the sample. Automatic cosmic ray removal option was utilized, with range of Raman spectra from 100 cm^{-1} to 1000 cm^{-1}. Fourier Transformed Infrared (FTIR) spectra were acquired on a Shimadzu IRPrestige-21 spectrophotometer, with 120 scans and spectral range from 400 to 4000 cm^{-1}. Absorbance measurements were obtained on a Shimadzu UV-2600 spectrophotometer in the

wavelength range from 200 to 800 nm and spectral resolution of 0.1 nm. The conversion of wavelength to energy scale for quantitative analysis was performed by using a Jacobian Conversion, outlined by Mooney & Kambhampati (2013) [33]. The band gap energy was determined using Tauc relation [34, 35]. Photoluminescence excitation and emission spectra were acquired using a Fluorolog 3-22 spectrometer (HORIBA Jobin-Yvon, Longjumeau, France) coupled with a 450 W xenon arc lamp, with a fixed emission of 453 nm and fixed excitation of 359 nm. The morphology and particle sizes of the prepared samples were observed using scanning electron microscope, SEM (Jeol JSM-6610LV), and Field emission scanning electron microscope, FE-SEM (FEI Quanta 250) for BMO:Tm-0. All measurements were taken at room temperature.

2.4. Thermoluminescence measurements

Thermoluminescence (TL) of 6 mg sample of pure and Tm^{3+}-doped (1% or 3%) powder $BaMoO_4$ samples were measured. A Risø TL/OSL reader, model DA-20, with a built-in $^{90}Sr/^{90}Y$ beta source with activity of 1.48 GBq was used. TL signal was detected by a photomultiplier tube EMI 9235QB (Bialkali) with better detection efficiency between 200 and 600 nm. Readouts were performed with samples exposed to beta radiation with doses ranging from 75 mGy to 750 mGy and non irradiated samples. Thermoluminescent signal was also registered for heating rates of 1 K/s, 3 K/s, 5 K/s and 10 K/s from 323 K to 773 K for a sample exposed to 300 mGy.

2.5. TL glow peak analysis

TL glow curves were analyzed according to the following methods:

2.5.1. Glow curve deconvolution

Computadorized Curve Deconvolution Analysis (CCDA) has been carried out by using the single glow-peak equation of general order kinetics [36]:

$$I(T) = I_m b^{\frac{b}{b-1}} exp\left(\frac{E}{kT}\frac{T-T_m}{T_m}\right) \times \left[(b-1)(1-\Delta)\frac{T^2}{T_m^2} exp\left(\frac{E}{kT}\frac{T-T_m}{T_m}\right) + Z_m\right]^{\frac{-b}{b-1}} \quad (1)$$

where $\Delta = \frac{2kT}{E}$, $\Delta_m = \frac{2kT_m}{E}$ and $Z_m = 1 + (b-1)\Delta_m$

In these expressions E is the trap depth, b, is the order of the kinetics, k, the Boltzmann's constant and T_m, the temperature corresponding to the maximum intensity of the peak. Curve fitting has been performed by using the software package Microsoft Excel, with Solver utility [37]. The goodness of fit was tested with the Figure of Merit (FOM) [38]:

$$FOM = \frac{\sum_p |TL_{exp} - TL_{fit}|}{\sum_p TL_{fit}} \tag{2}$$

where TL_{exp} corresponds to the experimental data and TL_{fit} to the fitted data points. The frequency factor (s) for general order kinetic glow peak is obtained by the relation [36]:

$$s = \frac{\beta E}{kT_m^2}\frac{1}{Z_m}exp\left(\frac{E}{kT_m}\right) \tag{3}$$

2.5.2. Peak shape method

The trap depth (E) was also calculated using the peak shape method with the methodology proposed by Chen as follows [39]:

$$E_\alpha = C_\alpha\left(k\frac{T_m^2}{\alpha}\right) - b_\alpha(2kT_m) \tag{4}$$

where α stands for τ,δ or ω. The constants c_α and b_α are given by [39]:

$c_\tau = 1.510 + 3.0(\mu - 0.42)$, $b_\tau = 1.58 + 4.2(\mu - 0.42)$

$c_\delta = 0.976 + 7.3(\mu - 0.42)$, $b_\delta = 0$

$c_\omega = 2.52 + 10.2(\mu - 0.42)$, $b_\omega = 1$

The parameters τ, δ and ω are given by: $\tau = T_m - T_1$, $\delta = T_2 - T_m$, $\omega = T_2 - T_1$

where T_m is the peak temperature at maximum height. T_1 and T_2 are the temperatures corresponding to half of the maximum intensities on either side of the glow peak maximum temperature (T_m) [39]. The geometrical shape parameter μ was calculated as $\mu = \delta/\omega$. Where $\mu = 0.42$ for first-order kinetics and $\mu = 0.52$ for second-order kinetics.

2.5.3. Variable heating rate method

The variable heating method relies on the analysis of the shift of thermoluminescent peak to higher temperatures when the heating rate is increased. Using the determined values of T_m at various heating rates (β), the trap depth (E) was determined with the following relation [39]:

$$ln(T_m^2/\beta) = ln(E/sk) + E/kT_m \tag{5}$$

The slope of straight line adjusted to the experimental data of $ln(T_m^2)/\beta$ vs. $1/kT_m$ provides the trap depth value.

3. Results and Discussions

To investigate the structure of prepared phosphors, X-ray diffraction (XRD) patterns were recorded as depicted in Figure 1. XRD patterns of $BaMoO_4$:Tm^{3+} synthesized by MAH method exhibit a scheelite-type crystalline structure of space group $I4_1/a$, without additional phases or impurities. All peaks observed in Figure 1a can be indexed to the tetragonal $BaMoO_4$ phase which is in agreement with standard data from JCPDS card No. 29-0193. Table 1 lists the main 2θ diffraction angles (and corresponding intensities), lattice parameters and crystallite sizes of $BaMoO_4$:Tm^{3+} samples and JCPDS 29-0193 standard data. The diffraction angles data are in good accordance with the JCPDS standard, and all expected peaks were detected in the experimental results.

From peak positions displayed in XRD, lattice parameters and unit cell sample volumes were calculated using the least-square refinement REDE93 program. The average sample crystallite diameter (D_{crys}) was determined using the (112) diffraction peak (2θ around 26.6^o) according to the Scherrer equation [40, 41]:

$$B = \frac{\kappa\lambda}{D_{crys}cos\theta} \tag{6}$$

where B is the full width at half maximum (FWHM), κ is the shape factor, λ is the wavelength of the Cu K_α radiation and θ is the Bragg angle.

The lattice parameters a and c for BMO:Tm-0, BMO:Tm-1 and BMO:Tm-3

Table 1: Crystallite diameter (Dcrys), band gap energy values (Eg), main diffraction angles and relative intensities of 100% diffraction peak (112), and lattice parameters of $BaMoO_4$ powders

Sample		JCPDS 29-0193	BMO:Tm-0	BMO:Tm-1	BMO:Tm-3
Crystalline Size (nm)[a]		–	47 ± 1	40 ± 2	46 ± 2
E_g		–	3.98	3.77	3.55
2θ intensity(^{o})(%)	(112)	26.53/100	26.68/100	26.46/100	26.64/100
	(004)	27.84/21	27.98/10	27.78/15	27.94/13
	(200)	32.07/30	32.22/33	32.00/28	32.20/35
	(204)	42.96/48	43.08/23	42.88/27	43.07/23
Lattice Parammeters	a=b(Å)	5.58	5.58	5.59	5.57
	c(Å)	12.82	12.80	12.84	12.80
	V_{cell} (nm^3)	0.399	0.398	0.401	0.398
	c/a	2.30	2.29	2.30	2.30

[a] Calculated using the (112), 100% diffraction peak.

powders synthesized using MAH method are close to the standart bulk material lattice parameters (a=5.5802 Å and c=12.821 Å) (JCPDS card no. 29-0193). Small differences can be related to small lattice distortions caused by residual stresses induced from preparation conditions, hydrotherm processing times and rare earth presence in the unit cell.

The unit cell volumes were calculated from the product of the lattice parameters, as in the scheelite crystalline structure type, $a = b$ and $volume = a \times a \times c$. Unit cell volumes were 0.398 nm^3, 0.401 nm^3 and 0.398 nm^3 for BMO:Tm-0, BMO:Tm-1 and BMO:Tm-3, respectively, values that are very similar to that of the JCPDS card (0.399 nm^3). Crystallite diameter (D_{crys}) calculated by using equation 6 were (47 ± 1) nm, (40 ± 2) nm and (46 ± 2) nm for BMO:Tm-0, BMO:Tm-1 and BMO:Tm-3, respectively. These results are close to the value of ≈ 52.2 nm presented by Adhikari et al (2013), and the range of 20-40 nm calculated by Yoon et al. (2006) [42, 43]. The $BaMoO_4$ primitive cell displays internal and external vibrational mode groups. Internal vibrations correspond to oscillations inside the $[MoO_4]^{2-}$ ionic molecular group with an immovable mass center and strong covalent Mo-O bonds. External or lattice phonons correspond to the Ba^{2+} cation motion and the rigid molecular unit $[MoO_4]^{2-}$ motions. The scheelite primitive cell presents 26 different vibration modes: $\Gamma = 3A_g + 5A_u + 5B_g + 3B_u + 5E_g + 5E_u$, but only A_g, B_g and E_g are Raman

Table 2: Raman frequencies (cm^{-1}) in $BaMoO_4$ powders doped with thulium ions.

Lattice mode Symmetry C_{4h}^6	$BaMoO_4$ (cm^{-1}) BMO:Tm-0	BMO:Tm-1	BMO:Tm-3	1100-1200^oC [a]	Assignments
A_g	892	891	890	892	$\nu_1(A_1)$
B_g	838	837	838	837	$\nu_3(F_2)$
E_g	791	791	791	791	
E_g	360	359	360	358	$\nu_4(F_2)$
B_g	346	345	345	345	
B_g	325	325	326	324	$\nu_2(E)$
A_g	325	325	326	324	
E_g	189	189	190	188	$\nu_{f,r}(F_1)$ free rotation
B_g	141	138	139	137	ν_{ext} - External
E_g				110	modes $[MoO_4]^{2-}$
B_g				76	and Ba^{2+} motions
E_g				74	

[a] Czocharalski [10]

active modes, while the odd ones ($4A_u$ and $4E_u$) can be registered only in the infrared spectra. The three B_u vibrations are silent modes; one A_u and one E_u modes are acoustic vibrations [44].

Characteristic Raman active mode peaks of $BaMoO_4$ scheelite structure are observed in Figure 1b and detailed in Table 2. The peaks correspond to external modes of $[MoO_4]^{2-}$ and $Ba^{2+}(Tm^{3+})$ motions, ext. ($2E_g$ and $1B_g$) are not observed, probably due to the fluorescence signal overlap of the samples [45, 46]. Three sets of defined peaks between 130 and 190 cm^{-1}, 320 and 360 cm^{-1}, and 790 and 900 cm^{-1} are observed in Raman spectra. The first region (130 to 190 cm^{-1}) corresponds to external modes ($1B_g$) and free rotation ($1E_g$) of $[MoO_4]^{2-}$ and Ba^{2+} or Tm^{3+} ions; the second region (320 to 360 cm^{-1}) corresponds to ν_2(E) and $\nu_4(F_2)$ ($2B_g$ $+1E_g$) of $[MoO_4]^{2-}$ and Ba^{2+} (or Tm^{3+} doped); and the third region (790 to 900 cm^{-1}) to ν_3 (F_2) and ν_1 (A_1) internal Raman modes associated with stretching vibrations of strong covalent Mo-O bonds of $[MoO_4]^{2-}$ ionic molecular group with an immovable mass center [44]. A frequency shifting of some peaks proportional to the concentration of the doped element (i.e., one-phonon-like behavior) and the splitting of a number of peaks involving different elements that share the same lattice site (i.e., two-phonon-like behavior), specially in materials with addition of dopant that modify crystalline lattice substantially, were expected, but weren't observed in these samples [47,

4].

The full width at half maximum (FWHM) values from Bragg reflections and Raman bands were calculated to determine a disorder degree at short- and intermediate-ranges of samples. The FWHM calculated values were very similar, 1 nm for Raman data and 0.03^o for XRD data, values close to the experimental error. These observations demonstrate that these materials have similar levels of deep defects probably because thermal treatments parameters were similar. However, these characterization techniques do not help the study of energy levels of the material.

The $[MoO_4]^{2-}$ ionic molecular group, characteristic of scheelite-type crystalline structures, observed in Raman and XRD data, can be confirmed by FTIR spectra. These spectra showed stretching in the region around 860 cm^{-1} and 790 cm^{-1} assigned to $F_2(3)$ antisymmetric and symmetric stretch vibrations, respectively, which are associated with the covalent Mo-O bonds stretching vibrations in a $[MoO_4]^{2-}$ tetrahedron [48, 49].

Figure 2a presents UV-Vis Absorbance spectra of $BaMoO_4$:Tm^{3+} samples obtained between 200 and 800 nm. BMO presents two fundamental absorption bands at 200-300 nm range, one around 260 nm (4.8 eV) and another band around 208 nm (6.0 eV). The band around 260 nm (4.8 eV) was attributed to electronic transitions within the $[MoO_4]^{2-}$ complex, according to Spassky et al. 2004 [50] and other results of research already published by our group [51, 52, 4]; these absorption bands are dislocated to higher wavelength values with increased concentration of Tm^{3+} ions in the crystalline lattice, similar to that observed by Adhikari et. al (2013) in $BaMoO_4$:Er^{3+} nanoparticles [42].

Inset of Figure 2a shows more details of absorbance bands in BMO:Tm-1 and BMO:Tm-3 samples. These absorbance bands around 358.5 nm, 464-472.5 nm, 662-699 nm, 773-794 nm correspond to $^3H_6 \rightarrow {}^1D_2$, $^3H_6 \rightarrow {}^1G_4$, $^3H_6 \rightarrow {}^3F_3$ and $^3H_6 \rightarrow {}^3H_4$ transitions of Tm^{3+} ion, respectively. BMO:Tm-3 presents one absorbance band at 523.5 nm, which could be atributed to both $^3H_6 \rightarrow {}^1G_4$ and $^3H_5 \rightarrow {}^1D_2$ transitions [53, 54].

The band gap energies of $BaMoO_4$:Tm^{3+} samples were calculated using Tauc

relation and are summarized in Table 1. The estimated band gap energies were found to be 3.98 eV, 3.77 eV and 3.55 eV for BMO:Tm-0, BMO:Tm-1 and BMO:Tm-3, respectively (Figure 2b), related to electronic transitions in $[MoO_4]^{-2}$ complex. The $BaMoO_4$:Tm^{3+} samples were produced in same temperature, consequently, a great difference in order-disorder was not expected, as previously discussed in the XRD and Raman results. However, with the increase of Tm^{3+} ions, an additional difference in morphology of particle surface was observed (Figure 3a-f). The surface atoms have unsatisfied valencies and, to reduce the surface energy, surface reconstruction occurs which leads to energy levels in the semiconductor's forbidden gap region. It is expected that band gap and trap concentration increase with a decrease in the particle size. Therefore the necessary energetic gap to occur electron-hole pair ($e' - h\cdot$) recombination can be variable [55].

With addition and increase of Tm^{3+} ion concentration in $BaMoO_4$, it was also expected an increase of atoms with unsatisfied valencies and, to reduce the local energy, localized reconstruction occurs, which leads to energy levels in the forbidden gap of the semiconductor, increasing the amount of traps [55]. In addition, the electronic transition $^3H_6 \rightarrow {}^1D_2$ of thulium ion, that proved to be dependent on its concentration, occurs around 359 nm, close to the band gap energy presented by BMO:Tm. The direct band gap by Tauc relation graph is plotted with $h\nu$ along the X-axis and $(h\nu\alpha)^2$ along the Y-axis, where $h\nu$ is energy of the photon and α is the absorption coefficient and the band gap is found by extrapolating the linear region of the curves to the X axis [34, 35]. Therefore, it is clear that the extrapolation of the curves linear region $(h\nu\alpha)^2$=0 (obtaining the band gap) is dependent of absorption and affected by thulium concentration. Consequently, the electron transition from valence band to conduction band can be favored with increase of Tm^{3+} ion concentration to 3% in crystalline lattice, shifting the absorption edge to lower energies in the visible electromagnetic spectra.

BMO:Tm samples with predominantly octahedral morphologies are visible in SEM (Scanning Electron Microscopy) micrographs (Figure 3). In the MAH

system, with a dominant liquid phase, the crystalline unit is free to grow in any direction (3D), therefore differences among morphologies of BMO:Tm samples are expected [52]. The high pressure during hydrothermal treatment and the presence of thulium doping in crystalline lattice induce modifications in the morphology. Figures 3(a,b) show superficial defects and distortions in micro-octahedra with a shortening and rounding of octahedral shapes, generating a hollow micro-ellipsoids structured BMO:Tm-0 sample as illustrated in the high resolution images (Figures 3(g,h)). Wang et. al. (2013) observed hollow structures in $SrMoO_4$ samples [56]. Micrographs of BMO:Tm-1 (Figures 3(c,d)) and BMO:Tm-3 (Figures 3(e,f)) show dense structure, keeping the characteristic octahedral morphology of molybdates obtained by MAH method, with aggregates of small particles, associated with the method and presence of thulium [1]. The presence of thulium causes the retention of octahedral morphology or the new formation of micro-octahedra; the increase in the amount of thulium in lattice leads to the growth of particles due to the formation of aggregates of smaller ones. As previously discussed, it is expected a variation on the band gap and on the amount of traps with presence of Tm^{3+} alio-valent doping and the variation of morphology of particles. Both smaller particle size and higher concentration of alio-valent Tm^{3+} induce formation of atoms with unsatisfied valences (in surface and in bulk, respectively), leading to an increase in the concentration of traps and a decrease in the band gap value. BMO:Tm-3 sample presents higher amount of alio-valent Tm^{3+} and larger particle size, therefore, it is expected that this sample presents higher concentration of traps and lower band gap value.

Figure 4a illustrates the excitation spectrum (PLE) of $BaMoO_4$:Tm^{3+}, λ_{EM}=453 nm at room-temperature. In PLE, the main peak observed at 359 nm in BMO:Tm-1 and BMO:Tm-3 is the characteristic excitation band related to the $^3H_6 \rightarrow {}^1D_2$ transition, confirming the UV-Vis absorbance spectra data previously discussed [53]. The peak at 359 nm is approximately 6 times more intense in BMO:Tm-3 than in BMO:Tm-1 samples. This fact supports the results observed

in band gap data and in absorbance spectra.

Figure 4b illustrates emission spectrum of $BaMoO_4$:Tm^{3+}, λ_{exc}=359 nm at room temperature. Photoluminescence (PL) spectra of BMO:Tm samples exhibits broad and low intensity band transitions related to $[MoO_4]^{2-}$, covering the visible region from 390 to 590 nm. PL spectra of BMO:Tm-1 and BMO:Tm-3 exhibit additional transitions due to thulium ions present in the molybdate matrix: the emission at 453 nm is assigned to $^1D_2 \rightarrow {}^3F_4$ transition of Tm^{3+}, [53, 57] and the energy corresponding to the peak at 545 nm is similar to the $^1D_2 \rightarrow {}^3H_{4,5}$ of Tm^{3+} transition (Figure 4c). Although the probability of this transition is modest, the increase of traps in the band gap could facilitate its appearance [58]. BMO:Tm-0 does not present these emissions assigned to Tm^{3+} ion.

Under the same measurement conditions, the $^3H_6 \rightarrow {}^1D_2$ transition at 453 nm in BMO:Tm-3 is approximately six times more intense that in BMO:Tm-1. This relation agrees with our previous discussion, in which the band gap of BMO:Tm-3 (3.55 eV) is closer to the applied excitation wavelength (3.69 eV) than the band gap of BMO:Tm-1 (3.77 eV), favoring electron-hole pair recombination and consequently increasing the intensity of photoluminescence. Furthermore, the presence of Tm^{3+} alio-valent ions induces a local increase of atoms with unsatisfied valences leading to an increase in the concentration of traps that act as recombination centers, amplifying the number of electron transition events from valence band to conduction band. As a consequence, the photoluminescence emission is favored for higher doping concentrations.

Figure 4d illustrates the CIE chromaticity diagram of $BaMoO_4$:Tm^{3+}. CIE parameters were calculated to estimate the change in the phosphor photometric characteristics with ion influence. The (x, y) chromaticity coordinates are (0.1657, 0.2137) for BMO:Tm-0; (0.1666, 0.2111) for BMO:Tm-1; and (0.1685, 0.1598) for BMO:Tm-3. The chromaticity diagram shows emission in the blue region for BMO:Tm-3 and in the greenish blue/blue region for the other two phosphors.

Thermoluminescence glow curves from samples irradiated with a 300 mGy

dose, measured at 5 K/s heating rate, are shown in Figure 5. Results show that pure BMO sample has a glow curve in the temperature range from 500 to about 700 K. BMO:Tm-1 exhibits a glow curve in the range from 500 to about 750 K, with maximum TL intensity at around 670 K. BMO:Tm-3 sample presents a rather well-defined TL glow curve with a main peak ($T_{max} \approx 450$ K), and a compound band at the 500-750 K range. The registered glow curve for BMO:Tm-3 is rather broad, extending over a large temperature range, which suggests the presence of multiple trap depths. The TL signal for the BMO:Tm-3 sample is much more intense than for the other compositions, suggesting the presence of a larger number of traps. Increasing the concentration of thulium ions from 1% to 3% in the $BaMoO_4$ matrix results in a significant increase of the TL emission. Additionally, the lower temperature of the glow peak for BMO:Tm-3 samples indicates that the traping centers are different for different doping levels.

Figure 6 shows the effect of the heating rate variation on the main TL peak registered for BMO:Tm-1 and BMO:Tm-3 samples. Data show a shift of the TL glow peak to higher temperatures with increase of heating rate, as expected.

Figure 7 shows TL glow curves measured from non-irradiated and irradiated BMO:Tm-3 samples. The comparison of the glow curves show that the exposure to 300 mGy and 750 mGy beta radiation doses results in a subtle variation on the main peak intensity and position. However, the intensity of the second peak located at temperatures higher than 570 K decreases for the irradiated samples. These outcomes point to a reduction of deeper traps due to the irradiation process. Results also show that the intensity of the BMO:Tm-3 glow curve is not affected by the radiation doses in this range of absorbed doses.

Figure 8 illustrates the deconvoluted TL glow curves, registered with a heating rate of 1 K/s, for both doped samples. Our curve fitting studies have shown that four isolated peaks are necessary to achieve an acceptable fit to the experimental glow curves. The fitting parameters are displayed in Table 3. The Figure of Merit (FOM) values are smaller than 2.4%, showing that experimental and fitted glow curves are in good agreement. The trap levels are in the energy

Table 3: Kinetic parameters of deconvoluted thermoluminescent peaks measured for BMO:Tm-1 and BMO:Tm-3 samples.

Sample	Peak	E (eV) Arrhenius	E(eV) Chen	Deconvolution (1 K/s) E(eV)	Frequency factor $[s(s^{-1})]$	b	Lifetime at 300 K
BMO:Tm-1	1	—	—	1.04	1.3×10^8	1.2	71 years
	2	1.2	1.13 ± 0.04	1.2	2.4×10^8	1.6	1.9×10^4 years
	3	1.28	1.25 ± 0.04	1.28	1.8×10^8	1.25	5.6×10^5 years
	4	1.34	1.3 ± 0.05	1.33	1.4×10^8	1.2	4.9×10^6 years
BMO:Tm-3	1	1.14	1.04 ± 0.04	0.92	5.8×10^9	2	5.7 days
	2	1.16	1.11 ± 0.04	1.02	1.1×10^{10}	2	140 days
	3	1.2	1.23 ± 0.04	1.14	7.4×10^8	2	614 years
	4	1.3	1.30 ± 0.05	1.24	2.1×10^8	1.2	1.04×10^5 years

range from about 0.92 to 1.33 eV for both samples. The frequency factors (s) associated with traps states for BMO:Tm-1 and BMO:Tm-3 are in the range from 10^8 s^{-1} to 10^{10} s^{-1}. Acceptable values of s are in the range from 10^8 to 10^{14} s^{-1} [27]. The frequency factor values are higher and have a larger range for the BMO:Tm-3 samples, more than 10-fold variation, contrasting with the 2-fold variation for BMO:Tm-1. This is consistent with the overall fitting results, as for similar values of activation energies, the TL peak temperatures are smaller for the BMO:Tm-3 samples than for the BMO:Tm-1 ones. At higher Tm^{3+} doping levels, higher trap concentrations are expected; also additional traps may be created, resulting in an increase on the intensity of luminescent signal. The b values in Table 3, related to the kinetic order of the glow peaks, correspond mainly to second order for the BMO:Tm-3 sample, indicating that the retraping probability is nearly the same as the recombination probability [25, 28].

The trap depth (activation energy) can also be determined through the Arrhenius method using various heating rates: a linear plot of $ln(T_m^2/\beta)$ *vs.* $1/kT_m$ is obtained, as shown in Figure 9. The slope of the straight line fitted to the experimental data corresponds to the trap depth (Table 3). Trap depth values calculated for all peaks by the glow curve method proposed by Chen are also displayed in Table 3. The activation energy values essentially agree with those calculated by different heating rate method and also by deconvolution procedure. The trap-depths calculated in this work for barium molybdate are similar to those calculated for lanthanum molybdate and gadolinium molybdate, both

doped with Tb^{3+} [26]. A simple diagram of band-gap values and trap depths for each sample is presented in Figure 10.

Table 3 provides the charge carriers expected lifetime in each trapping level for BMO:Tm-1 and BMO:Tm-3 at room temperature (T = 300 K). The expected trapping level lifetime corresponds to the time required for the TL peak intensity to be reduced by a factor $1/e$ of its initial value [59]. Using the kinetic parameters discussed above, the expected lifetime (τ) associated to each TL peak at room temperature was calculated from the equation [27]:

$$\tau = s^{-1} exp\left(\frac{E}{kT}\right) \tag{7}$$

where s is the frequency factor and k is the Boltzmann constant. Results displayed in table 3 show that the mean charge lifetime for all TL peaks from the BMO:Tm-1 sample are longer than seventy years. Thus the time required for release and recombination of trapped electrons in the BMO:Tm-1 trapping levels is too large to be useful in persistent luminescence, in accordance with the glow-peak temperatures observed for this sample [27, 32]. For BMO:Tm-3 sample, the combination of s and E values results in expected lifetimes higher than 140 days for traps corresponding to the TL peaks 2, 3 and 4, which are also too long to be useful in persistent luminescence. The results calculated for peak 1 from BMO:Tm-3 lie in the zone relevant to persistent luminescence [27]. For peak 1 (BMO:Tm-3) the expected trapping level lifetime, at room-temperature (300 K), is around 5.7 days. Table 4 exhibits the kinetic parameters and calculated expected lifetime for peak 1 of BMO:Tm-3 glow curves measured with all the experimental heating rates and the values are very similar. Column 5 (Table 4) presents the FOM values for each heating rate. The lifetime calculated for peak 1 of BMO:Tm-3 is consistent with a possible persistent luminescence emission mechanism from this trapping level. However, the observation of persistent luminescence by this material needs further theoretical and experimental investigation and it's beyond the scope of the present work.

Table 4: Deconvolved Kinetic parameters for peak 1 from BMO:Tm-3 with four heating rates.

Heating rate (K/s) (β)	E (eV)	Frequency factor [$s(s^{-1})$]	b	Lifetime at 300 K	FOM
1	0.92	5.8×10^9	2	5.7 days	2.3%
3	0.93	7.8×10^9	2	6.2 days	2.7%
5	0.94	1.1×10^{10}	2	6.5 days	2.8%
10	0.98	5.56×10^{10}	2	6.0 days	2.6%

4. Conclusions

We have synthesized $BaMoO_4$:Tm^{3+} powders by the co-precipitation method and grown in a microwave-assisted hydrothermal system. The structural, optical and luminescence properties were determined by means of several characterization methods such as XRD, Raman spectroscopy, Scanning Electron Microscope (SEM), Fourier Transformed Infrared spectra (FTIR), absorbance spectra, photoluminescence (PL) and thermoluminescence (TL). XRD and Raman studies of $BaMoO_4$:Tm^{3+} powders provide evidence of a scheelite-type crystalline structure. The optical emission for the BMO:Tm-3 sample occurs in the blue region ($^1D_2 \rightarrow {}^2F_4$ transitions from Tm^{3+} ions) whereas BMO:Tm-0 and BMO:Tm-1 phosphors emit in the greenish blue/blue region. TL glow curves of the phosphors provide evidence that the increase of Tm^{3+} ions in the $BaMoO_4$ matrix results in a larger concentration of trapping levels inside the band-gap, and it's in full agreement with the observed decrease in band gap values and the increase in photoluminescence emission. The analysis of the kinetic parameters, determined from thermoluminescent glow curves, points to a possible persistent luminescence emission in the BMO:Tm-3 sample. This material can be a potential blue-light or near UV long-lasting phosphor, although more studies about the luminescent behavior of $BaMoO_4$:Tm^{3+} compounds are needed in order to investigate the luminescence lifetime and the possibility of applications of this compound.

5. Acknowledgements

The authors would like to thank Prof. Dr. N. S. Gonçalves and Profa. Dra. L. C. Courrol from DQ-UNIFESP-Diadema and DF-UNIFESP-Diadema, respectively, for contributions with Raman and photoluminescence measurements, and Profa. Dra. R. S. Coimbra of CEME-UNIFESP-São Paulo for contributions with FE-SEM measurements. They also acknowledge the São Paulo Research Foundation (FAPESP) for grants #2016/20578-5, #2013/07437-5, #2010/16437-0, #2010/06816-4 and Conselho Nacional de Desenvolvimento Científico e Tecnológico (CNPq).

References

[1] M. F. C. Abreu, F. V. Motta, R. C. Lima, M. S. Li, E. Longo, A. P. A. Marques, Effect of process parameters on photophysical properties and barium molybdate phosphors characteristics, Ceramics International 40 (5) (2014) 6719–6729. doi:10.1016/j.ceramint.2013.11.134.

[2] S. Cho, Photoluminescence properties of $BaMoO_4$:RE^{3+} (RE = Eu, Sm, Dy, Tb, Tm) phosphors, J. Korean Phys. Soc. 69 (2016) 1479–1484. doi:10.3938/jkps.69.1479.

[3] L. K. Bharat, S. H. Lee, J. S. Yu, Synthesis, structural and optical properties of $BaMoO_4$:Eu^{3+} shuttle like phosphors, Mater. Res. Bull. 53 (2014) 49–53. doi:10.1016/j.materresbull.2014.02.002.

[4] A. P. A. Marques, F. C. Picon, D. M. A. Melo, P. S. Pizani, E. R. Leite, J. A. Varela, E. Longo, Effect of the order and disorder of $BaMoO_4$ powders in photoluminescent properties, J. Fluoresc 18 (2008) 51–59. doi:10.1007/s10895-007-0237-6.

[5] Z. Xia, D. Chen, Synthesis and luminescence properties of $BaMoO_4$:Sm^{3+} phosphors, J. Am. Ceram. Soc 93 (2010) 1397–1401. doi:10.1111/j.1551-2916.2009.03574.x.

[6] X. Yang, J. Liu, H. Yang, X. Yu, Y. Guo, Y. Zho, J. Liu, Synthesis and characterization of new red phosphors for white led applications, J. Mater. Chem 19 (2009) 3771–3774. doi:10.1039/B819499H.

[7] J. Li, H. Yan, F. Yan, A novel high color purity blue-emitting phosphor:$CaBi_2B_2O_7$:Tm^{3+}, Mater. Sci. Eng. B 209 (2016) 56–59. doi:10.1016/j.mseb.2016.03.004.

[8] B. Han, J. Zhang, P. J. Li, H. Z. Shi, $KKBaBP_2O_8$:Tm^{3+}: a novel blue emitting phosphor with high color purity, JETP Letters 99 (2014) 561–564. doi:10.1134/S0021364014100063.

[9] N. Giri, K. Mishra, S. Rai, Upconversion based tunable white-light generation in Ln:Y_2O_3 nanocrystalline phosphor (Ln = Tm/Er/Yb), J. Fluoresc 21 (2011) 1951–1958. doi:10.1007/s10895-011-0894-3.

[10] L. Guerbous, M. Derbal, J. P. Chaminade, Photoluminescence and energy transfer of Tm^{3+} doped Li in $(WO_4)_2$ blue phosphors, J. Lumin. 130 (2010) 2469–2475. doi:10.1016/j.jlumin.2010.08.014.

[11] E. H. Song, S. Ding, M. Wu, S. Ye, Z. T. Chen, Y. Y. Ma, Q. Y. Zhang, Tunable white upconversion luminescence from Yb^{3+}-$Tm^{3+}Mn_{2+}$ tri-doped perovskite nanocrystals, Opt Mater Express 4 (6) (2014) 1186–1196. doi:10.1364/OME.4.001186.

[12] S. Gao, C. Sun, Y. Ji, Z. Zhu, Y. Wang, Z. You, Y. Wang, J. Feng, S. Lv, H. Wang, C. Tu, Photoluminescence properties and white emission of Dy^{3+}, Tm^{3+}: NaY $(WO_4)_2$ phosphors, Mater. Express 3 (2) (2013) 127–134. doi:10.1166/mex.2013.1107.

[13] J. Hu, X. H. Gong, Y. J. Chen, J. H. Huang, Y. F. Lin, Z. D. Luo, Y. D. Huang, Tunable luminescence of Dy^{3+} single-doped and Dy^{3+}/Tm^{3+} co-doped tungsten borate glasses, Opt. Mater. 38 (2014) 108–112. doi:10.1016/j.optmat.2014.09.034.

[14] J. Liao, B. Qiu, H. Wen, J. Chen, W. You, L. Liu, Synthesis process and luminescence properties of Tm^{3+} in AWO_4 (A = Ca, Sr, Ba) blue phosphors, J. Alloy Compd. 487 (2009) 758–762. doi:10.1016/j.jallcom.2009.08.068.

[15] K. V. den Eeckhout, P. F. Smet, D. Poelman, Persistent luminescence in rare-earth codoped $Ca_2Si_5N_8$:Eu^{2+}, J. Alloy Compd 129 (10) (2009) 1140–1143. doi:10.1016/j.jlumin.2009.05.007.

[16] T. Aitasalo, D. Hreniak, J. Höls Persistent luminescence of $Ba_2MgSi_2O_7$:Eu^{2+}, J. Lumin 122–123 (2007) 110–112. doi:10.1016/j.jlumin.2006.01.112.

[17] J. Randall, M. Wilkins, Phosphorescence and electron traps. ii. the interpretation of long-period phosphorescence, P. Roy. Soc. Lond. A 184 (1945) 390–407. doi:10.1098/rspa.1945.0025.

[18] H. F. Brito, O. M. L. Malta, M. C. F. C. Felinto, E. E. de Sousa Teotonio, The chemistry of metal enolates, Patai series: the chemistry of functional groups, CHICHESTER: WILEY, United Kingdom, 2009.

[19] T. Aitasalo, J. Hölsä, H. Jungner, M. Lastusaari, J. Niittykoski, M. Parkkinen, R. Valtonen, Eu^{2+} doped calcium aluminates prepared by alternative low temperature routes, Opt. Mater 26 (2) (2004) 113–116. doi:10.1016/j.optmat.2003.11.007.

[20] H. F. Brito, J. Hassinen, J. Hölsä, H. Jungner, T. Laamanen, M. Lastusaari, M. Malkamäki, J. Niittykoski, P. Nov Optical energy storage properties of $Sr_2MgSi_2O_7$:Eu^{2+}, R^{3+} persistent luminescence materials, J. Therm. Anal. Calorim 105 (2) (2011) 657–662. doi:10.1007/s10973-011-1403-2.

[21] R. Hahn, S. Berger, P. Schmuki, Bright visible luminescence of self-organized ZrO_2 nanotubes, J. Solid State Electrochem 14 (2) (2010) 285–288. doi:10.1007/s10008-008-0748-3.

[22] H. F. Brito, J. Hölsä, T. Laamanen, M. Lastusaari, M. Malkamäki, L. C. V. Rodrigues, Persistent luminescence mechanisms: human imagination at work, Opt Mater Express 2 (4) (2012) 371–381. doi:10.1364/OME.2.000371.

[23] E. G. Yukihara, S. W. S. McKeever, Optically Stimulated Luminescence: Fundamentals and Applications, 1st Edition, J. Wiley, Singapore, 2011.

[24] E. G. Yukihara, E. Okuno, On the thermoluminescent properties and behaviour of brazilian topaz, Nucl. Instr. Meth. Phys. Res. B 141(1–4) (1998) 514–517. doi:10.1016/S0168-583X(98)00041-X.

[25] K. V. den Eeckhout, A. Bos, D. Poelman, P. F. Smet, Revealing trap distribution in persistent phosphors, Phys. Rev. B 87 (4) (2013) 045126:1–11. doi:10.1103/PhysRevB.87.045126.

[26] S.Dutta, S. Som, J.Priya, S.K.Sharma, Band gap, cie and trap depth parameters of rare earth molybdate phosphors for optoelectronic applications, Solid. State Sci 18 (2013) 114–122. doi:10.1016/j.solidstatesciences.2013.01.012.

[27] M. Mashangva, M. Singh, T. Singh, Estimation of optimal trapping parameters relevant to persistent luminescence, Indian J. Pure Appl. Phys 49 (2011) 583–589.

[28] K. V. den Eeckhout, D. Poelman, P. Smet, Persistent luminescence in Non Eu^{2+} doped compounds: a review, Materials 6 (2013) 2789–2818. doi:10.3390/ma6072789.

[29] K. V. den Eeckhout, P. Smet, D. Poelman, Persistent luminescence in Eu^{2+}-doped compounds: a review, Materials 3 (2010) 2536–2566. doi:10.3390/ma3042536.

[30] Y. Li, M. Gecevicius, J. Qiu, Long persistent phosphors from fundamentals to applications, Chem. Soc. Rev 45 (2016) 2090–2136. doi:10.1039/C5CS00582E.

[31] Z. Pan, Y. Lu, F. Liu, Sunlight-activated long-persistent luminescence in the near-infrared from Cr^{3+} doped zinc gallogermanates, Nat. Mater 11 (2012) 58–63. doi:10.1038/nmat3173.

[32] B. Liu, C. Shi, Z. Qi, Potential white-light long-lasting phosphor: Dy^{3+}-doped aluminate, Appl. Phys. Lett 86 (19) (2005) 191111:1–191111:3. doi:10.1063/1.1925778.

[33] J. Mooney, P. Kambhampati, Get the basics right: Jacobian conversion of wavelength and energy scales for quantitative analysis of emission spectra, J. Phys. Chem. Lett 4 (19) (2013) 3316–3318. doi:10.1021/jz401508t.

[34] V. Kolobanov, I. Kamenskikh, V. Mikhailin, I. Shpinkov, D. Spassky, B. Zadneprovsky, L. Potkin, G. Zimmerer, Optical and luminescent properties of anisotropic tungstate crystals, Nucl. Instr. and Meth. A 486 (2002) 496–503. doi:10.1016/S0168-9002(02)00760-X.

[35] D. Wood, J. Tauc, Weak absorption tails in amorphous semiconductors, Phys. Rev. B: Condens. Matter 5 (8) (1972) 3144–3151. doi:10.1103/PhysRevB.5.3144.

[36] G. Kitis, J. M. Gomez-Ros, J. W. N. Tuyn, Thermoluminescence glow-curve deconvolution functions for first, second and general orders of kinetics, J. Phys. D: Appl. Phys. 31 (1998) 2636–2641. doi:10.1088/0022-3727/31/19/037.

[37] D. Afouxenidis, G. S. Polymeris, N. C. Tsirliganis, G. Kitis, Computerised curve deconvolution of tl/osl curves using a popular spreadsheet program, Radiat. Prot. Dosim. 149 (4) (2012) 363–370. doi:10.1093/rpd/ncr315.

[38] H. Balian, N. Eddy, Figure-of-merit (FOM), an improved criterion over the normalized chi-squared test for assessing goodness-of-fit of gamma ray spectral peaks, Nucl. Instr. Meth. 145 (4) (1977) 389–395. doi:10.1016/0029-554X(77)90437-2.

[39] V. Pagonis, G. Kitis, C. Furetta, Numerical and Practical Exercises in Thermoluminescence, Springer-Verlag, New York, 2006.

[40] G. Hitoki, T. Takata, S. Ikeda, M. Hara, J. Kondo, M. Kakihana, K. Domen, Mechano-catalytic overall water splitting on some mixed oxides, Catal. Today 145 (2–4) (2000) 175–181. doi:10.1016/S0920-5861(00)00457-0.

[41] J. Langford, A. Wilson, Scherrer after sixty years: A survey and some new results in the determination of crystallite size, J. Appl. Cryst. 11 (2) (1978) 102–113. doi:10.1107/S0021889878012844.

[42] R. Adhikari, G. Gyawali, T. Kim, T. Sekino, S. Lee, Synthesis of Er^{3+} loaded barium molybdate nanoparticles: A new approach for harvesting solar energy, Mater. Lett. 91 (2013) 294–297. doi:10.1016/j.matlet.2012.10.004.

[43] J. Yoon, J. Ryu, K. Shim, Photoluminescence in nanocrystalline $MMoO_4$ (M = Ca, Ba) synthesized by a polymerized complex method, Mat Sci Eng B-Solid 127 (2–3) (2006) 154–158. doi:10.1016/j.mseb.2005.10.015.

[44] T. Basiev, A. Sobol, Y. Voronko, P. Zverev, Spontaneous raman spectroscopy of tungstate and molybdate crystals for raman lasers, Opt. Mater. 15 (3) (2000) 205–216. doi:10.1016/S0925-3467(00)00037-9.

[45] M. Claybourn, M. Ansell, Using raman spectroscopy to solve crime: inks, questioned documents and fraud, Sci Justice 4 (4) (2000) 261–271. doi:10.1016/S1355-0306(00)71996-4.

[46] W. Romão, N. Schwab, M. Bueno, Forensic chemistry: perspective of new analytical methods applied to documentoscopy, ballistic and drugs of abuse, Quim. Nova 34(10) (4) (2011) 1717–1728. doi:10.1590/S0100-40422011001000005.

[47] M. Moura, A. Ayala, I. Guedes, M. Grimsditch, C. Loong, L. Boatner, Raman scattering study of $Tb(V_{1-x}P_x)O_4$ single crystals, J. Appl. Phys 95 (3) (2004) 1148–1151. doi:10.1063/1.1640461.

[48] A. A. Marques, D. Melo, C. Paskocimas, P. Pizani, E. Leite, E.Longo, Photoluminescent $BaMoO_4$ nanopowders prepared by complex polymerization method (CPM), J. Solid. State Chem 179 (3) (2006) 671–678. doi:10.1016/j.jssc.2005.11.020.

[49] K. Nakamoto, Infrared and Raman Spectra of Inorganic and Coordination Compounds, Wiley, New York, 1986.

[50] D. Spassky, S. Ivanov, V. Kolobanov, V. Mikhailin, V. Zemskov, B. Zadneprovski, L. Potkin, Optical and luminescent properties of the lead and barium molybdates, Radiat. Meas 38 (4–6) (2004) 607–610. doi:10.1016/j.radmeas.2004.03.019.

[51] A. P. A. Marques, D. M. A. Melo, C. A. Paskocimas, P. S. Pizani, E. R. Leite, E. Longo, Focus on Solid State Chemistry, Nova Science Publishers, Inc., New York, 2006.

[52] A. Marques, M. Tanaka, E. Longo, E. Leite, I. Rosa, The role of the Eu^{3+} concentration on the $SrMoO_4$:Eu phosphor properties: Synthesis, characterization and photophysical studies, J. Fluoresc. 21 (3) (2011) 893–899. doi:10.1007/s10895-010-0604-6.

[53] A. Huignard, A. Aron, P. Aschehoug, B. Viana, J. Théry, A. Laurent, J. Perrière, Growth by laser ablation of Y_2O_3 and Tm:Y_2O_3 thin films for optical applications, J. Mater. Chem. 10 (2000) 549–554. doi:10.1039/A904710G.

[54] E. E. Dunaeva, P. G. Zverev, M. E. Doroshenko, A. V. Nekhoroshikh, L. I. Ivleva, V. V. Osiko, Growth and spectral-luminescent study of $SrMoO_4$ crystals doped with Tm^{3+} ions, Dokl. Phys. 61 (3) (2016) 119–123. doi:10.1134/S1028335816030058.

[55] T. Pradeep, Nano: The essentials, Understanding Nanoscience and Nanotechnology, McGraw-Hill, New York, 2007.

[56] Y. Wang, P. Yang, P. Ma, F. Qu, S. Gai, N. Niu, F. Hea, , J. Lin, Hollow structured $SrMoO_4$:Yb^{3+}, Ln^{3+} (Ln = Tm, Ho, Tm/Ho) microspheres: tunable up-conversion emissions and application as drug carriers, J. Mater. Chem. B 1 (2013) 2056–2065. doi:10.1039/C3TB00377A.

[57] L. G. V. Uitert, R. R. Soden, Emission spectra of trivalent thulium, J. Chem. Phys. 34(1) (1) (1961) 276–279. doi:10.1063/1.1731577.

[58] G. Poirier, V. A. Jerez, C. B. de Arajo, Y. Messaddeq, S. J. L. Ribeiro, M. Poulain, Optical spectroscopy and frequency upconversion properties of Tm^{3+} doped tungstate fluorophosphate glasses, J. Appl. Phys. 93(3) (2003) 1493–1497. doi:10.1063/1.1536017.

[59] J. L. L. R. Chen, V. Pagonis, Evaluated thermoluminescence trapping parameters - what do they really mean?, Radiat. Meas. 91 (2016) 21–27. doi:10.1016/j.radmeas.2016.04.006.

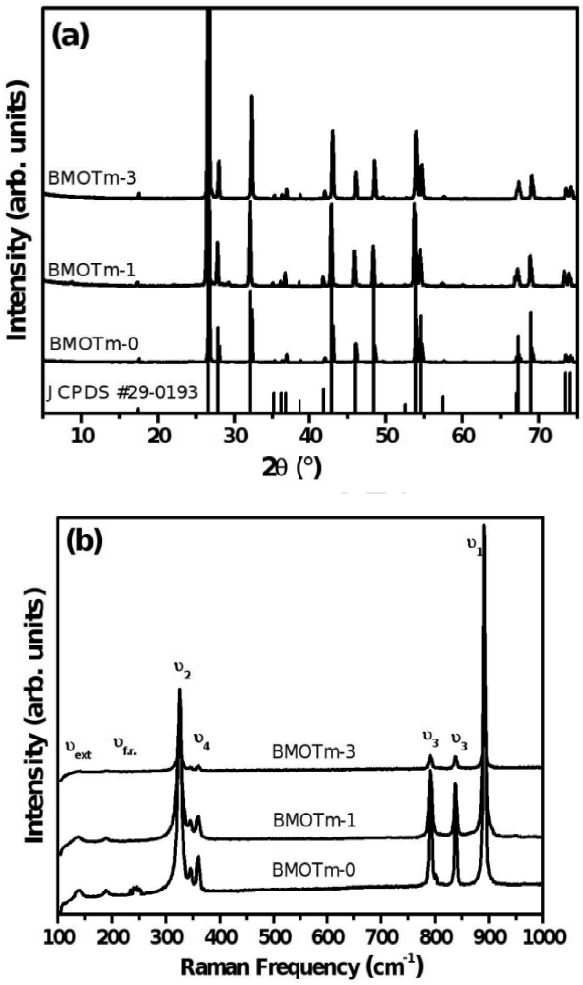

Figure 1: (a) XRD pattern and (b) Raman spectra of BMO:Tm-0, BMO:Tm-1 and BMO:Tm-3.

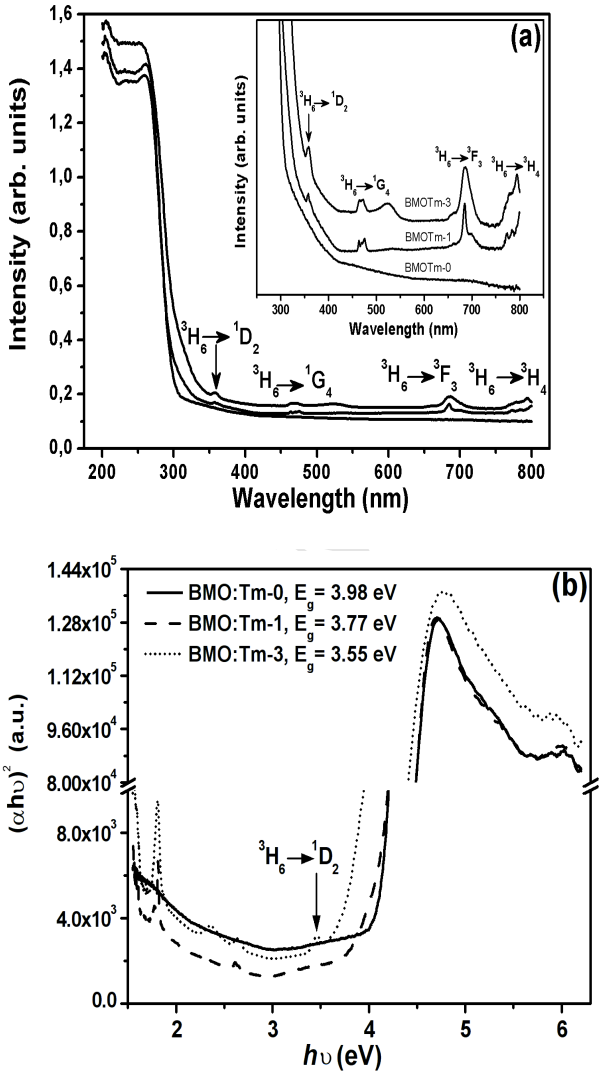

Figure 2: (a) UV-Vis diffuse reflectance spectra of BMO:Tm^{3+} samples and (b) Band gap energies obtained using the Tauc relation.

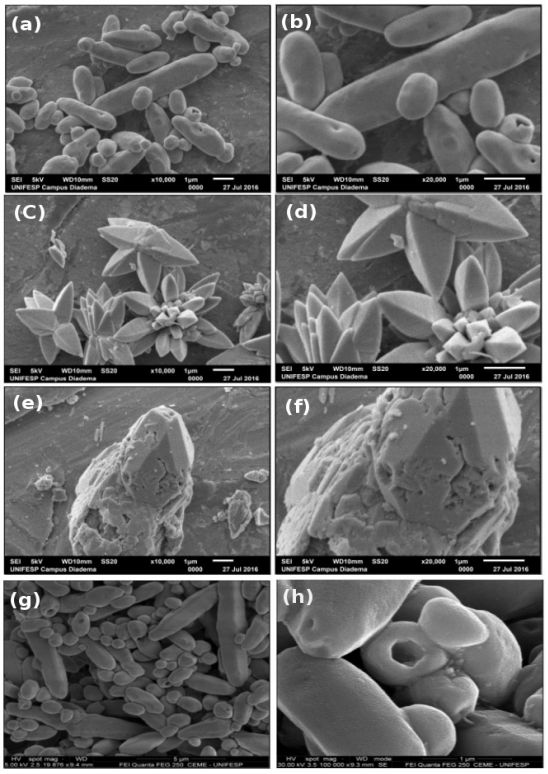

Figure 3: SEM images of the BMO:Tm-0 (a-b), BMO:Tm-1 (c-d) and BMO:Tm-3 (e-f). High resolution FE-SEM images from BMO:Tm-0 (g,h)

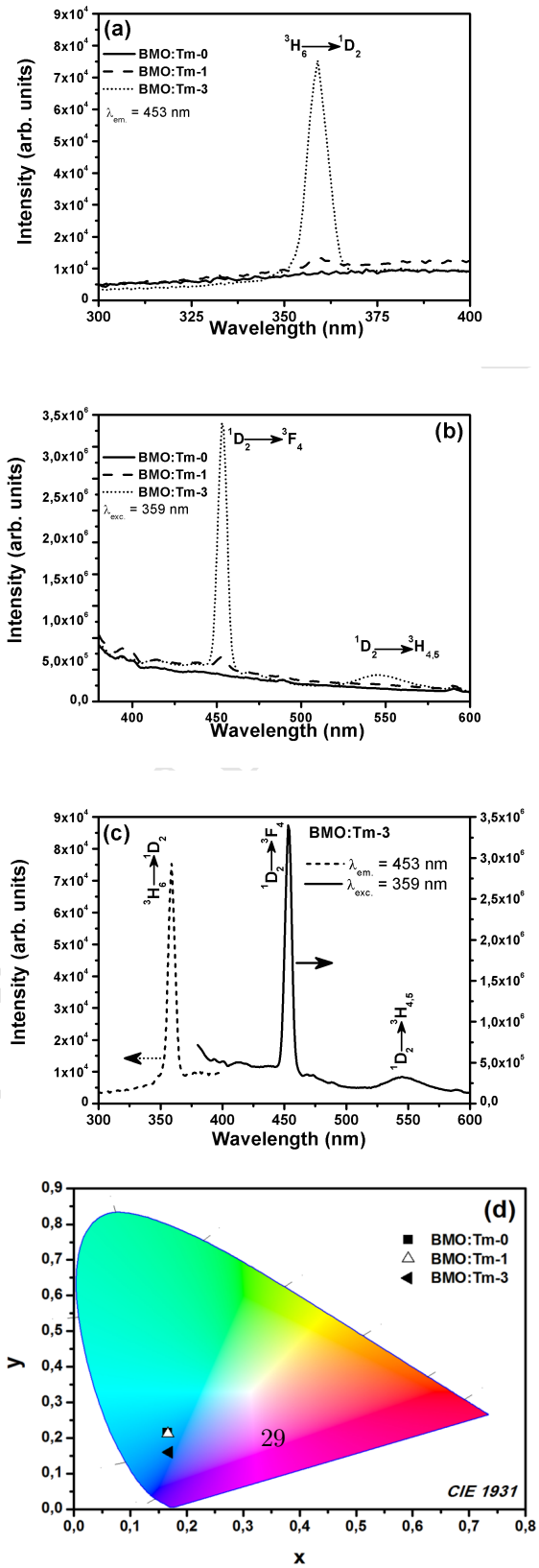

Figure 4: (a) Excitation and (b) emission spectra of $BaMoO_4$ doped with Tm^{3+}, (c) Excitation and emission spectra of BMO doped with 3%Tm and (d) CIE chromaticity diagram.

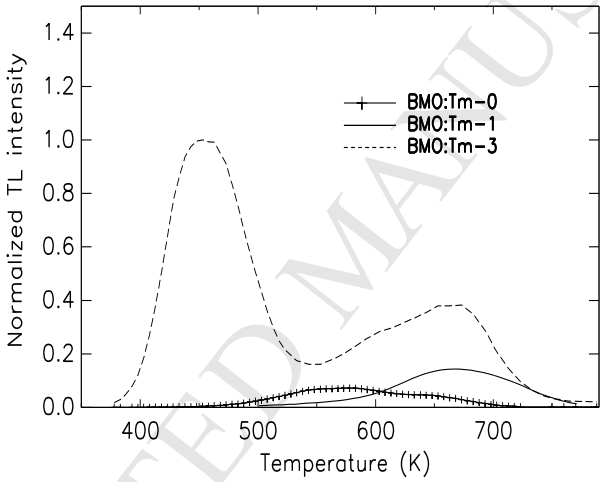

Figure 5: Glow curves of BMO:Tm-0, BMO:Tm-1 and BMO:Tm-3, registered with a heating rate of 5 K/s.

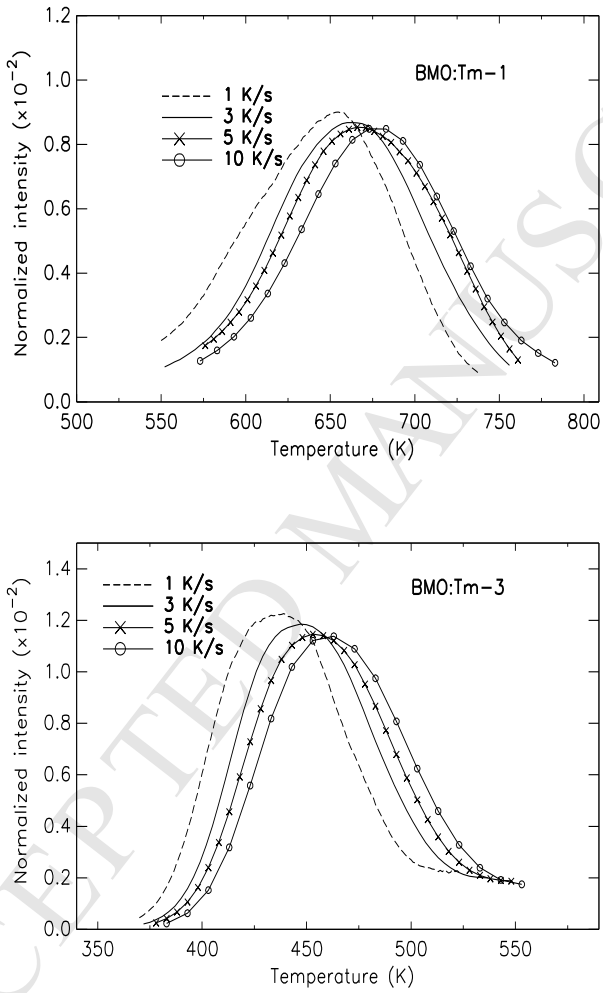

Figure 6: Illustration of heating rate effect on the main TL peak for BMO:Tm-1 and BMO:Tm-3. The data are normalized to unit area.

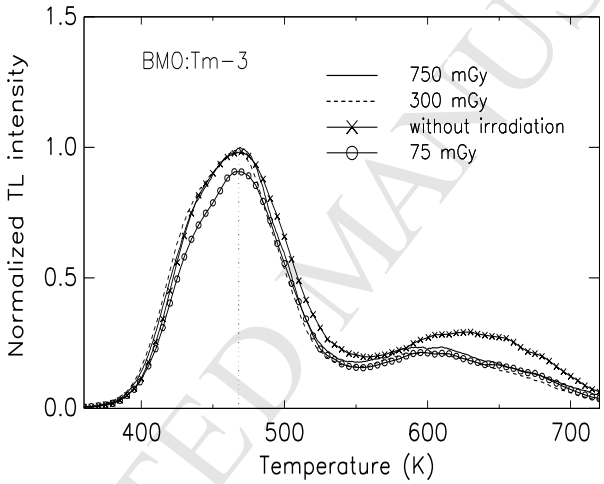

Figure 7: Glow curves for BMO:Tm-3 without irradiation and irradiated with 750 mGy, 300 mGy and 75 mGy beta doses, obtained at a heating rate of 5K/s.

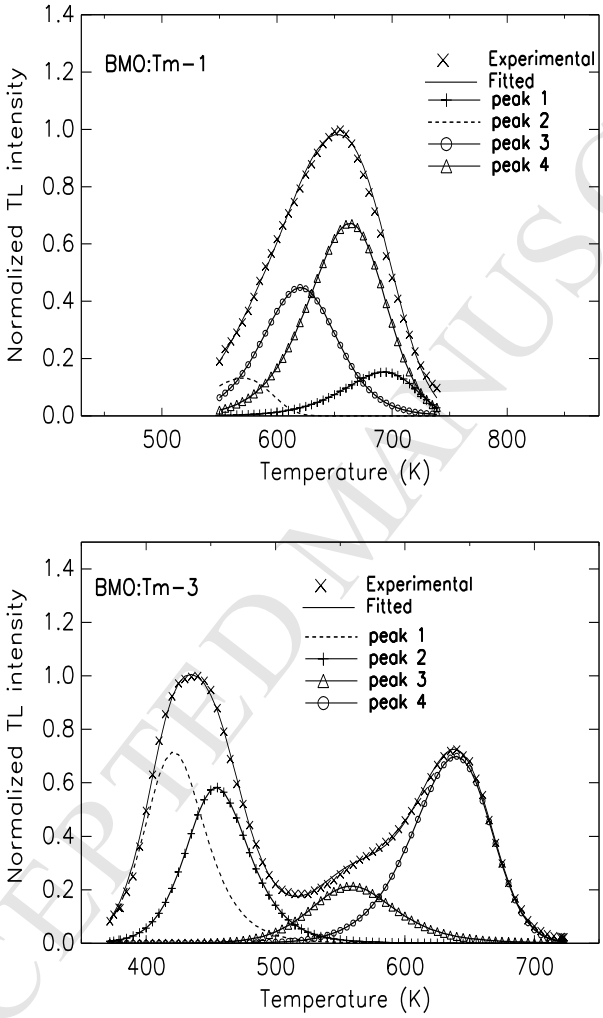

Figure 8: Deconvoluted thermoluminescent glow curves for BMO:Tm-1 and BMO:Tm-3. The FOM values are 2.4% and 2.1%, respectively. The heating rate was 1 K/s.

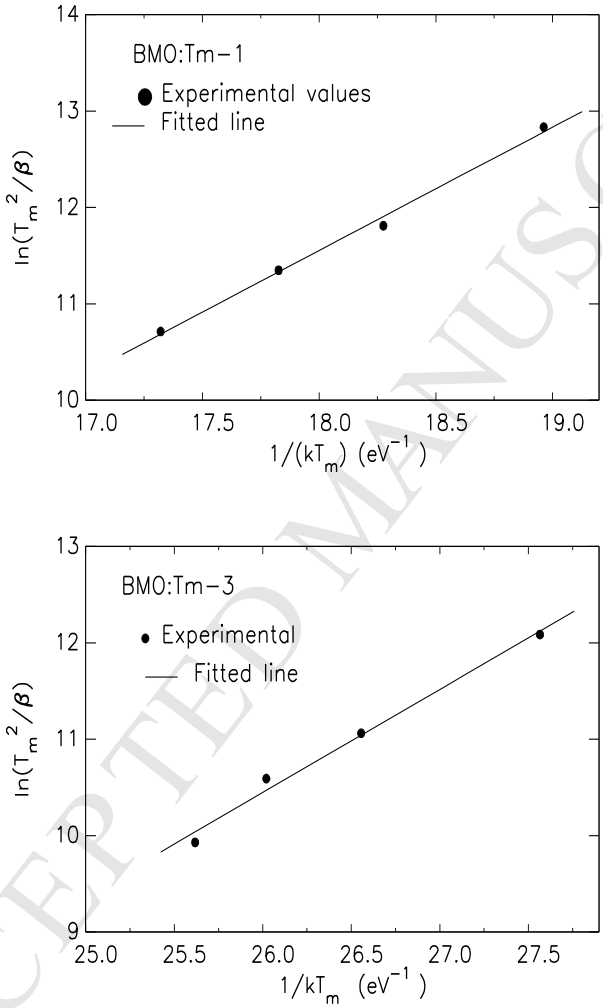

Figure 9: Plot of $ln(T_m^2/\beta)$ *vs.* $1/kT_m$ corresponding to the position of peak 3 of the BMO:Tm-1 sample and peak 1 of the BMO:Tm-3 sample for the experimental glow curves.

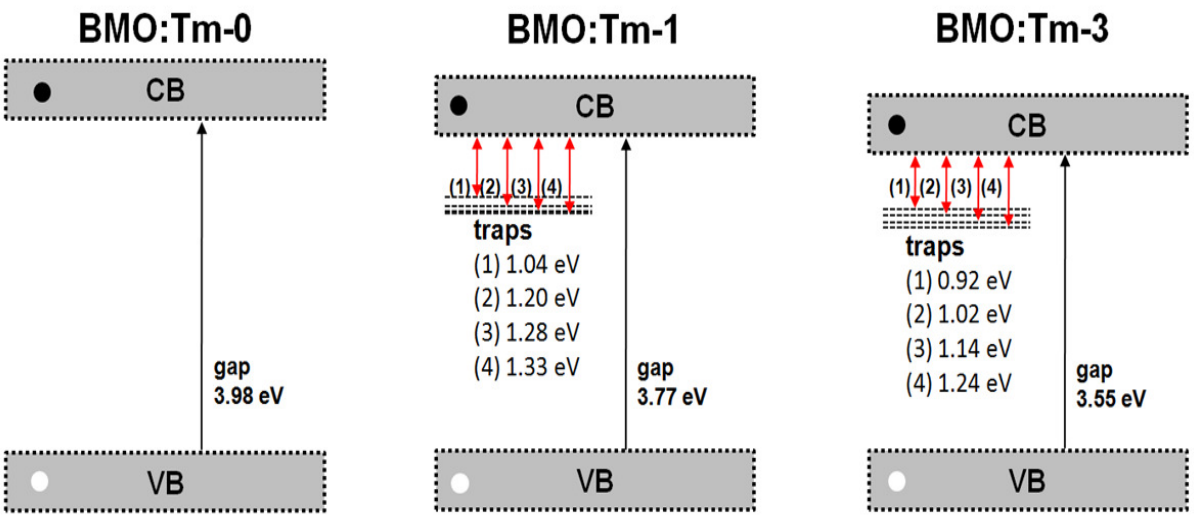

Figure 10: Band-gap and traps levels structure of BMO:Tm-0, BMO:Tm-1 and BMO:Tm-3.

Highlights

- $BaMoO_4:Tm^{3+}$ powders were synthesized by a co-precipitation method and grown in a microwave-assisted hydrothermal system.
- A scheelite-type crystalline structure was identified from XRD and Raman studies.
- Band-gap, trap levels energy and lifetime depends on the thulium concentration.
- The trap level lifetime, for the sample doped with 3% thulium, is consistent with the persistent luminescence phenomenon.